Direct calculation of effective mobile ion concentration in lithium superionic conductors

Check for updates

Bowei Pu[1], Zheyi Zou[2] ✉, Jinping Liu[1], Bing He [3], Dezhi Chen[2], Da Wang[1], Yue Liu[3], Maxim Avdeev [4,5] &
Siqi Shi [1,6] ✉

In the realm of lithium superionic conductors, pursuing higher ionic conductivity is imperative, with the variance in lithium-ion concentration playing a determining role. Due to the permanent and temporary site-blocking effects, especially at non-dilute concentrations, not all Li-ions contribute to ionic conductivity. Here, we propose a strategy to directly calculate effective mobile ion concentration in which multiple-ion correlated migration is considered in the percolation analysis with the input of Li-ion distributions and hopping behavior based on kinetic Monte Carlo simulation, termed P-KMC. We provide examples of two representative lithium superionic conductors, cubic garnet-type $Li_xA_3B_2O_{12}$ ($0 \leq x \leq 9$; A and B represent different cations) and perovskite-type $Li_xLa_{2/3-x/3}TiO_3$ ($0 \leq x \leq 0.5$), to demonstrate the direct dependence of the ionic conductivity on the effective mobile ion concentration. This methodology provides a robust tool to identify the optimal compositions for the highest ionic conductivity in superionic conductors.

Superionic conductors with high ionic conductivity are critical components of solid-state devices such as solid-state batteries and electrochemical sensors[1–6]. These materials are typically composed of mobile ions and a semi-rigid vibrating framework[7–10]. In certain materials, such as garnet $Li_{7-x}La_3Zr_{2-x}Ta_xO_{12}$, perovskite $Li_xLa_{2/3-x/3}TiO_3$ and NASICON $Li_{1+x}Al_xTi_{2-x}(PO_4)_3$, the lithium-ion concentrations can be adjusted within a certain range through aliovalent ion substitution, and the ionic conductivities are highly correlated with the ion concentrations[10–18]. In order to determine the optimal composition for achieving the highest ionic conductivity, it is essential to establish a definitive link between Li-ion concentration and ionic conductivity.

Due to the permanent and temporary site-blocking effects, not all the Li ions can contribute to the ionic conductivity. On the one hand, some Li ions may be permanently blocked by framework ions in localized regions. For example, in perovskite $Li_{0.5}La_{0.5}TiO_3$ where Li-ion, La ion, and vacancy partially occupy the same crystallographic site, some of the Li ions may be blocked by La ions in adjacent sites[12]. Excluding the permanently blocked ions, the remaining Li ions that have the potential for long-range migration are denoted as mobile ions, also referred to as accessible ions[19]. On the other hand, a fraction of mobile ions may be temporarily blocked by other mobile ions during the diffusion process. This phenomenon arises because, within a

specific arrangement of mobile ions over a period of time, there may not be sufficient vacancies for ion hopping[17,20]. For example, in cubic garnet $Li_7La_3Zr_2O_{12}$, numerous Li ions are immobile due to the temporary blockage, while only the remaining Li ions capable of jumps can be classified as effective mobile ions[20,21]. Therefore, it is crucial to identify which Li ions are effective mobile ions and which ones constitute the blocked ions, and further investigate their impacts on the ionic conductivity. For convenience, the definitions of the different types of Li ions and their concentrations are summarized in Section S1 of the Supplementary Material, including Li-ion concentration (C_{Li}), mobile ion concentration (C_m), and effective mobile ion concentration (C_e).

The percolation theory, which is concerned with the connectivity of discrete sites, can be employed to elucidate the site-blocking effects in ion transport[19,22,23]. Current percolation methods are typically applied on random distributions and assume only uncorrelated single-ion jumps[19]. However, in many superionic conductors, Li ions adhere to specific distribution rules, and multiple-ion correlated migration is known to play a critical role, especially at non-dilute concentrations, which have been confirmed by dynamic methods such as molecular dynamics (MD) simulations and kinetic Monte Carlo (KMC) simulations[24–31]. Consequently, in percolation analysis, it is necessary to consider specific Li-ion distributions and

[1]State Key Laboratory of Materials for Advanced Nuclear Energy & School of Materials Science and Engineering, Shanghai University, Shanghai, China. [2]School of Materials Science and Engineering, Xiangtan University, Xiangtan, China. [3]School of Computer Engineering and Science, Shanghai University, Shanghai, China. [4]School of Chemistry, The University of Sydney, Sydney, NSW, Australia. [5]Australian Nuclear Science and Technology Organisation, Sydney, NSW, Australia. [6]Materials Genome Institute, Shanghai University, Shanghai, China. ✉e-mail: zyzou@xtu.edu.cn; sqshi@shu.edu.cn

their hopping behavior[32]. Among the dynamic methods, KMC simulations provide an efficient way to obtain reasonable Li-ion distributions and hopping behavior with acceptable accuracy and low computational cost[32–36]. By utilizing these outcomes as input parameters for percolation analysis, the accuracy and rationality of percolation analysis can be significantly enhanced.

In this work, we propose a strategy, termed P-KMC, that combines an improved percolation analysis with KMC simulations to directly calculate effective mobile ion concentration. The KMC simulations generate reasonable Li-ion distributions and hopping behavior which serve as input parameters for percolation analysis, and then the effective mobile ions and blocked ions are directly identified through the percolation analysis, which takes into account multiple-ion correlated migration when determining conduction state. We apply this method to two representative lithium superionic conductors, cubic garnet-type $Li_xA_3B_2O_{12}$ ($0 \leq x \leq 9$; A and B represent different cations)[37–39] and cubic perovskite-type $Li_xLa_{2/3-x/3}TiO_3$ ($0 \leq x \leq 0.5$)[12,40–45]. Our results show that the effective mobile ion concentration (C_e) exhibits the same trend vs. Li content (x) as the ionic conductivities in these two examples, highlighting the close association and predictability of C_e to ionic conductivity.

Results

Workflow of P-KMC method

The workflow of the P-KMC method is illustrated in Fig. 1. First, the lattice-gas model of the input crystal structure is constructed through topological analysis (Fig. 1a). Then, KMC simulations are performed to obtain ion trajectories (Fig. 1b), from which reasonable Li-ion distributions and hopping behavior can be extracted. Finally, the percolation analysis is performed on every distribution sample, and the effective mobile ion concentration

(C_e) can be obtained by averaging the results of all percolation analyses (Fig. 1c).

Cubic garnet

We demonstrate the applicability of P-KMC method in two representative lithium superionic conductors, cubic garnet $Li_xA_3B_2O_{12}$ ($0 \leq x \leq 9$; where A and B represent a series of aliovalent cations, such as A = La and B = Zr for $Li_7La_3Zr_2O_{12}$) and cubic perovskite $Li_xLa_{2/3-x/3}TiO_3$ ($0 \leq x \leq 0.5$). The former exhibits the site-blocking effects of adjacent Li ions, while the latter exhibits the site-blocking effect of both adjacent Li ions and framework ions (La ions). The influence of the variation of Li content (x) on the ionic conductivity is assessed using the effective mobile ion concentration (C_e) as a proxy.

For cubic garnet $Li_xA_3B_2O_{12}$, the lattice-gas model is constructed based on the Li-ion diffusion pathways, which involve the interconnections between tetrahedral and octahedral sites[46]. Each tetrahedral site is surrounded by four octahedrally coordinated sites, each octahedral site is surrounded by two tetrahedrally coordinated sites, and all sites are partially occupied by Li ions, as depicted in Fig. 2a, b. We disregard the effect of framework element substitution and perform KMC simulations in a $2 \times 2 \times 2$ supercell based on the cubic $Li_7La_3Zr_2O_{12}$ crystal structure at 300 K, accommodating a maximum of 576 Li ions (equivalent to Li content $x = 9$, Li-ion concentration $C_{Li} = 3.275 \times 10^{28} \, m^{-3}$, supercell volume $V = 1.759 \times 10^{-26} \, m^3$). Although the theoretical maximum Li content reaches $x = 9$ per formula unit when all Li sites are occupied by Li ions[32], it has been suggested that mutual locking of adjacent tetrahedral and octahedral sites imposes an upper bound of $x \leq 7.5$[38]. Figure 2b illustrates a typical distribution of Li ions in the two-dimensional topological pathways, showcasing the temporary site-blocking effect in the diffusion process. To

Fig. 1 | Workflow of the P-KMC method.
a Construction of lattice-gas model. Note that the two-dimensional model depicted here is only for simplified demonstration and is not the model utilized in actual simulations. **b** KMC simulations to obtain reasonable distributions and hopping behavior of Li ions. **c** Percolation analysis to identify effective mobile ions and blocked ions. Effective mobile ion is the Li-ion within long-range bidirectional percolated pathways, while blocked ion is immobile or can only be percolated in one direction. They satisfy the relationship: $N_{Li} = N_e + N_b$, where N_{Li}, N_e and N_b denote the number of Li ions, effective mobile ions and blocked ions, respectively. And $N_b = N_p + N_t$, where N_p and N_t are the number of permanently blocked ions and temporarily blocked ions, respectively.
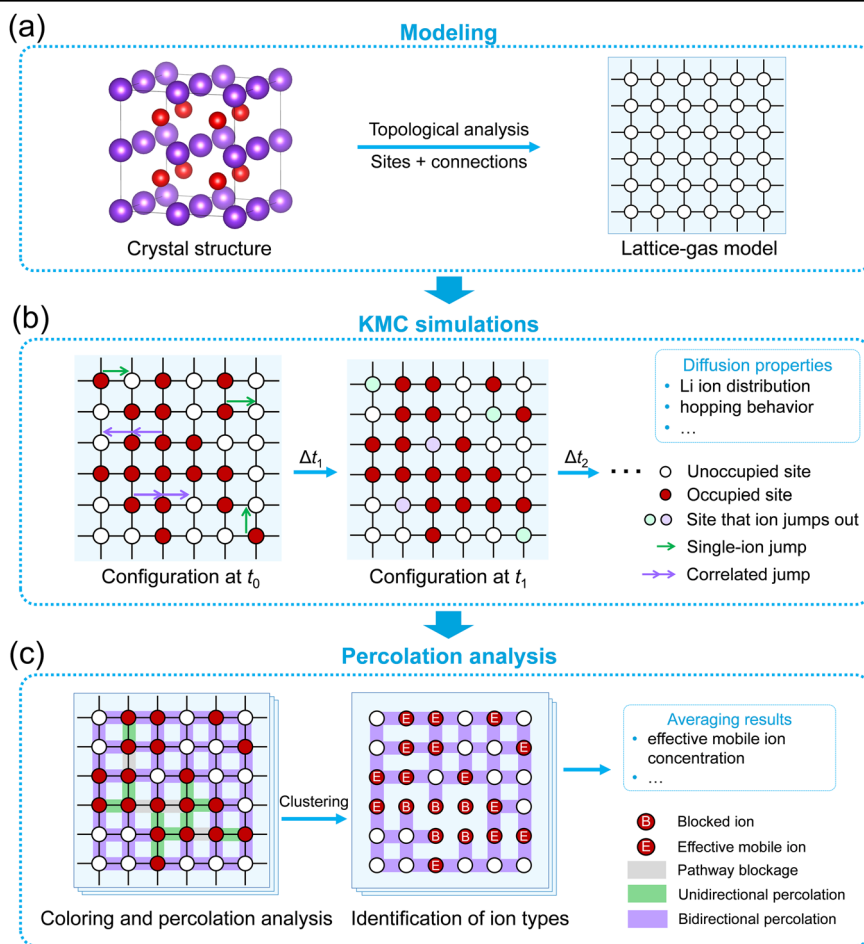
Fig. 2 | The Li–O polyhedra, topological pathways and comparison of C_{Li}, C_e and experimental ionic conductivity (σ_{exp}) in cubic garnet structure.
a Li–O polyhedra in the crystal structure. **b** Different types of ions and pathways identified through percolation analysis. **c** The comparison of the varying trends of C_{Li}, C_e and the experimental ionic conductivity (σ_{exp}) relative to Li content (x_{Li}) in garnet structures. The simulation conditions are $E_{nn} = 0.06$ eV, $\Delta E_{site} = 0.12$ eV and $T = 300$ K. The insert plot provides a more direct comparison of C_e and σ_{exp} after normalization, demonstrating a high R^2 value of 0.901. The values of σ_{exp} are adapted from the following compositions: $Li_3Er_3Te_2O_{12}$, $Li_5La_3Bi_2O_{12}$, $Li_6La_3Zr_{1.5}W_{0.5}O_{12}$, $Li_{6.2}La_3Zr_{1.2}Sb_{0.8}O_{12}$, $Li_{6.4}La_3Zr_{1.4}Ta_{0.6}O_{12}$, $Li_{6.5}La_3Zr_{1.75}Te_{0.25}O_{12}$, $Li_{6.75}La_3Zr_{1.75}Ta_{0.25}O_{12}$, $Li_7La_3Zr_2O_{12}$ and $Li_{7.5}La_{2.5}Sr_{0.5}Zr_2O_{12}$, all of which are measured at room-temperature except for $Li_3Er_3Te_2O_{12}$ (measured at 450 °C) due to the measurement difficulty of its negligible room-temperature ionic conductivity[13,16,39].
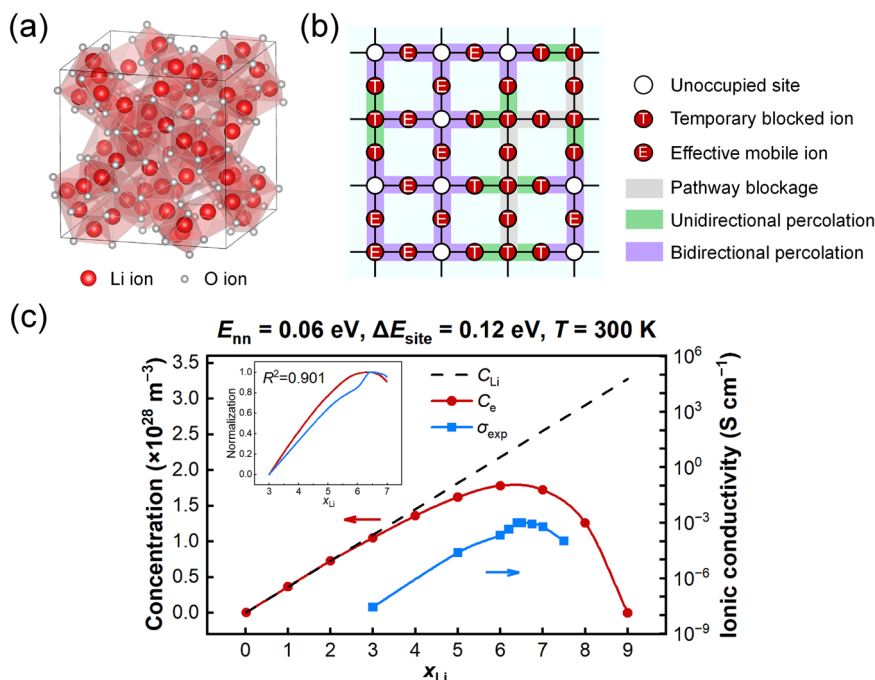

Table 1 | Input parameters and output results of P-KMC simulations for the garnet system of $x = 7$ and $T = 300$ K

Inputs		Outputs	
Model name	$Li_7A_3B_2O_{12}$	Percentage of single-ion jump (P_1)	71.36%
Li-ion content (x)	7	Percentage of two-ion correlated jump (P_2)	26.83%
Li-ion concentration (C_{Li})	$2.54 \times 10^{28}\,m^{-3}$	Percentage of three-ion correlated jump (P_3)	1.59%
Temperature (T)	300 K	Percentage of four-ion correlated jump (P_4)	0.21%
Nearest-neighbor interaction energy (E_{nn})	0.06 eV	Effective mobile ion concentration (C_e)	$1.72 \times 10^{28}\,m^{-3}$
Occupation energy of tetrahedral site	0.00 eV		
Occupation energy of octahedral site	0.12 eV		
Equilibration MCS	1000		
Production MCS	10000		
Supercell size	$2 \times 2 \times 2$		

elucidate the details of the P-KMC simulations, Table 1 summarizes the input parameters and output results for the simulation system with $x = 7$ and $T = 300$ K, corresponding to the formula $Li_7A_3B_2O_{12}$. For simplicity, the values of energy parameters E_{nn} and ΔE_{site} required by KMC simulation (see "Methods" section for detailed introduction) are assigned as 0.06 and 0.12 eV, respectively, which are approximately 2.3 and 4.6 k_BT (when $T = 300$ K) in the Arrhenius equation, and the energy values remain consistent across all simulated concentrations. The results indicate a very low proportion of correlated jumps involving more than two ions (1.81%), and therefore, the percolation analysis only considers single-ion jumps (71.36%) and two-ion correlated jumps (26.83%) when evaluating the percolated state. The correlated jump percentage reported here is consistent with that found in literature[28], which is approximately 25%.
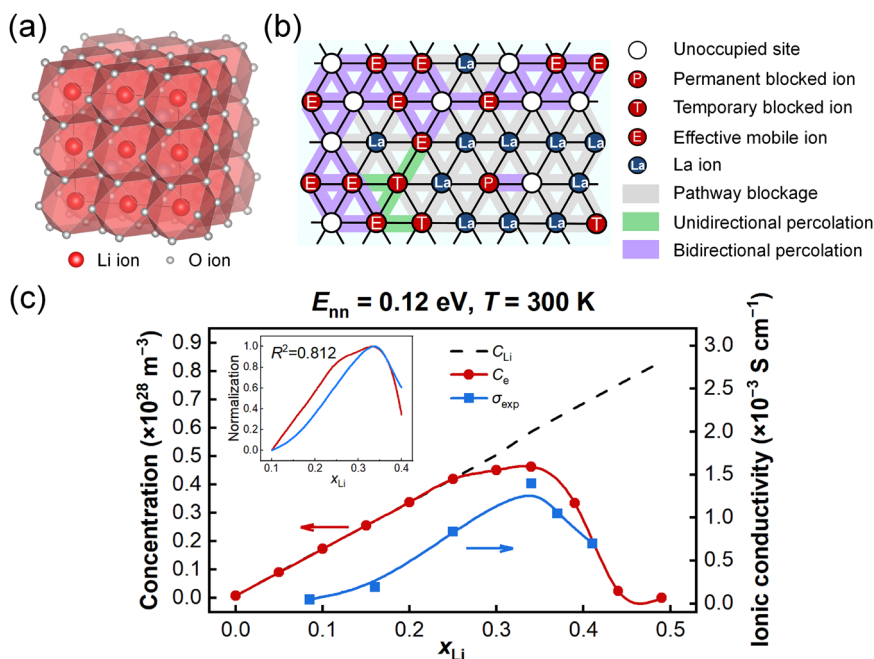
Figure 2c reveals that the difference between C_{Li} and C_e is not significant in the dilute concentration region ($x \leq 3$). However, as x increases, the gap between these two values widens, and the relationship $C_e \leq C_{Li}$ is consistently observed, as indicated by the red solid line (C_e) and black dashed line (C_{Li}). This phenomenon is primarily attributed to the blocking effect and the enhanced correlation of ion jumps at high x region. Previous studies[39] suggest that $x > 3$ is necessary to achieve significant ionic

conductivity in garnet solid electrolytes, where the Li-ion concentration becomes non-dilute according to the divergence between C_{Li} and C_e, highlighting the importance of distinguishing between these two concentrations in garnet structures. Hence, C_e, rather than C_{Li}, can serve as an estimation of the ionic conductivity in a superionic conductor, as it contains much more information about ion diffusion properties. The trend of C_e is consistent with that of the room-temperature ionic conductivity in the experimentally available x range of garnet structures (with $R^2 = 0.901$ after normalization)[39], indicating the strong predictive capability of C_e for ionic conductivity. Additionally, the maximum value of C_e appears at $x = 6$–7, which deviates from the trend of C_{Li}, suggesting a significant blocking effect at this point, which is similar to Morgan's previous results[32].

Cubic perovskite

Figure 3 illustrates a schematic depiction of the second example, cubic perovskite $Li_xLa_{2/3-x/3}TiO_3$ ($0 \leq x \leq 0.5$)[12,40–43], following the general chemical formula ABO_3 ($A = Li$, La; $B = Ti$). In perovskite structure, the AO_{12} cages, referred to as A-cages, are hosted in the framework of corner-sharing BO_6 octahedra, with each A-cage adjacent to six face-sharing neighboring A-cages. The lattice-gas model is constructed based on the Li-ion diffusion

Fig. 3 | The Li–O polyhedra, topological pathways and comparison of C_{Li}, C_e and σ_{exp} in cubic perovskite structure. a Li–O polyhedra in the crystal structure. **b** Different types of ions and pathways identified through percolation analysis. **c** The comparison of varying trends of C_{Li}, C_e and σ_{exp} relative to x_{Li} in perovskite structures at room-temperature. The simulation conditions are $E_{nn} = 0.12$ eV and $T = 300$ K. Since there is only one non-equivalent sites in the structure, $\Delta E_{site} = 0$. The insert plot provides a more direct comparison of C_e and σ_{exp} after normalization, demonstrating a high R^2 value of 0.812. The values of σ_{exp} are adapted from $Li_x La_{2/3-x/3} TiO_3$[18].

pathways in perovskite structure, which involve the interconnections of A-cages[46]. La ions are mixed occupied with Li ions in A-cages, serving as blockages in the pathways. In this work, for the sake of simplicity, the blocked sites (La ions) are randomly chosen with a fixed content of 0.5, and the impact of element substitution is not taken into account. The KMC simulations are performed in an $8 \times 8 \times 8$ supercell based on the cubic $Li_{0.5}La_{0.5}TiO_3$ crystal structure with a maximum of 256 Li ions (equivalent to $x = 0.5$, $C_{Li} = 0.850 \times 10^{28}$ m^{-3}, $V = 2.968 \times 10^{-26}$ m^3) at 300 K. Figure 3b shows a typical arrangement of Li and La ions, elucidating the temporary and permanent site-blocking effects in perovskite structure. An example of the input parameters and output results for the simulation system with $x = 0.34$ and $T = 300$ K ($Li_{0.34}La_{0.553}TiO_3$) is presented in Table S2 of the Supplementary Material. Given that there is only one non-equivalence symmetric site in the simulated perovskite structure, ΔE_{site} is set to 0. The parameter E_{nn} holds a value of 0.12 eV, corresponding to approximately 4.6 $k_B T$ ($T = 300$ K), across all simulated concentrations. Figure 3c presents the dependence of C_{Li} and C_e on x, confirming the proposed relationship $C_{Li} \geq C_e$. The values of C_{Li} and C_e are almost equal when $x \leq 0.25$, but their difference becomes increasingly larger when $x > 0.25$, indicating high ion correlation in non-dilute concentrations. The peak value of C_e occurs around $x = 0.34$, after which C_e begins to decrease. The parabolic variation of C_e corresponds to that of the room-temperature ionic conductivities (σ_{exp}) within the experimentally available range of x in perovskite structures (with $R^2 = 0.812$ after normalization), revealing the close association between C_e and σ_{exp}[12,47].

Discussion

A deeper understanding of the relationship between effective mobile ion concentration and ionic conductivity is provided in Section S4 of the Supplementary Material. The aforementioned examples demonstrate that within a certain range, an increase in Li-ion concentration is beneficial for increasing effective mobile ion concentration. However, beyond this range, further increases in concentration can lead to the obstruction of diffusion pathways due to the site-blocking effect, thereby inhibiting ion jumps. The strategy of enhancing ionic conductivity by optimizing Li-ion concentration, as explored in many previous studies[16–18], is, in fact, a process of increasing ionic conductivity by increasing the effective mobile ion concentration. The P-KMC method can identify the optimal Li-ion concentration where the effective mobile ion concentration reaches its

maximum, which serves as an indicator for the highest ionic conductivity. Two approaches can be proposed to optimize ionic conductivity by increasing effective mobile ion concentration. The first approach is to regulate the Li-ion concentration. As illustrated in Fig. 2c, our P-KMC method indicates that the optimal Li content range for garnet structures is $x = 6$–7. This can be achieved through aliovalent substitution[10]. This strategy has also been applied to rhombohedral NASICON structures, where increasing Na content is found to facilitate correlated migration, thereby promoting Na ion mobility[24]. Another approach is to adjust the interactions between Li ions (E_{nn}) and between Li ions and framework ions (E_{site}), as demonstrated in Eq. (1) in the "Methods" section. Although there has been no experimental investigation on the direct tuning of E_{nn} and E_{site} for LLZO and LLTO, a reversible octahedral-to-tetrahedral migration of Cr in $Li_{1.2}Mn_{0.2}Ti_{0.4}Cr_{0.2}O_2$, observed by EXAFS spectroscopy, has been found to significantly affect the interaction energies by changing the coordination environment of the ions, resulting in a boost of effect mobile ion concentration[48].

In summary, we present an efficient and informative scheme to directly calculate the effective mobile ion concentration in superionic conductors by combining kinetic Monte Carlo simulation and static percolation analysis (P-KMC). Our method not only facilitates the quantitative determination of effective mobile ion concentrations but also enables the evaluation of its effect on ionic conductivity. We believe that the P-KMC method can be applied to other solid electrolytes or electrodes, as long as the migration of mobile ions in these materials can be abstracted as the motion of particles in a lattice-gas model. A suggestion of subsequent work is to accurately compute the energy parameters (E_{site}, E_{nn}, energy barrier), ion distributions, and hopping behavior for KMC simulations and percolation analysis, which can be obtained through bond valence site energy (BVSE) calculations, first-principles calculations, and molecular dynamics simulations[24,26,35,36,49].

Methods
Kinetic Monte Carlo simulation
The pathway networks for Li-ions, which consist of sites and connections, are represented by a lattice-gas model through topological analysis of crystal structure[46,50–52]. In KMC simulations, the total energy of the configuration is expressed as the sum of the interactions between Li ions and framework
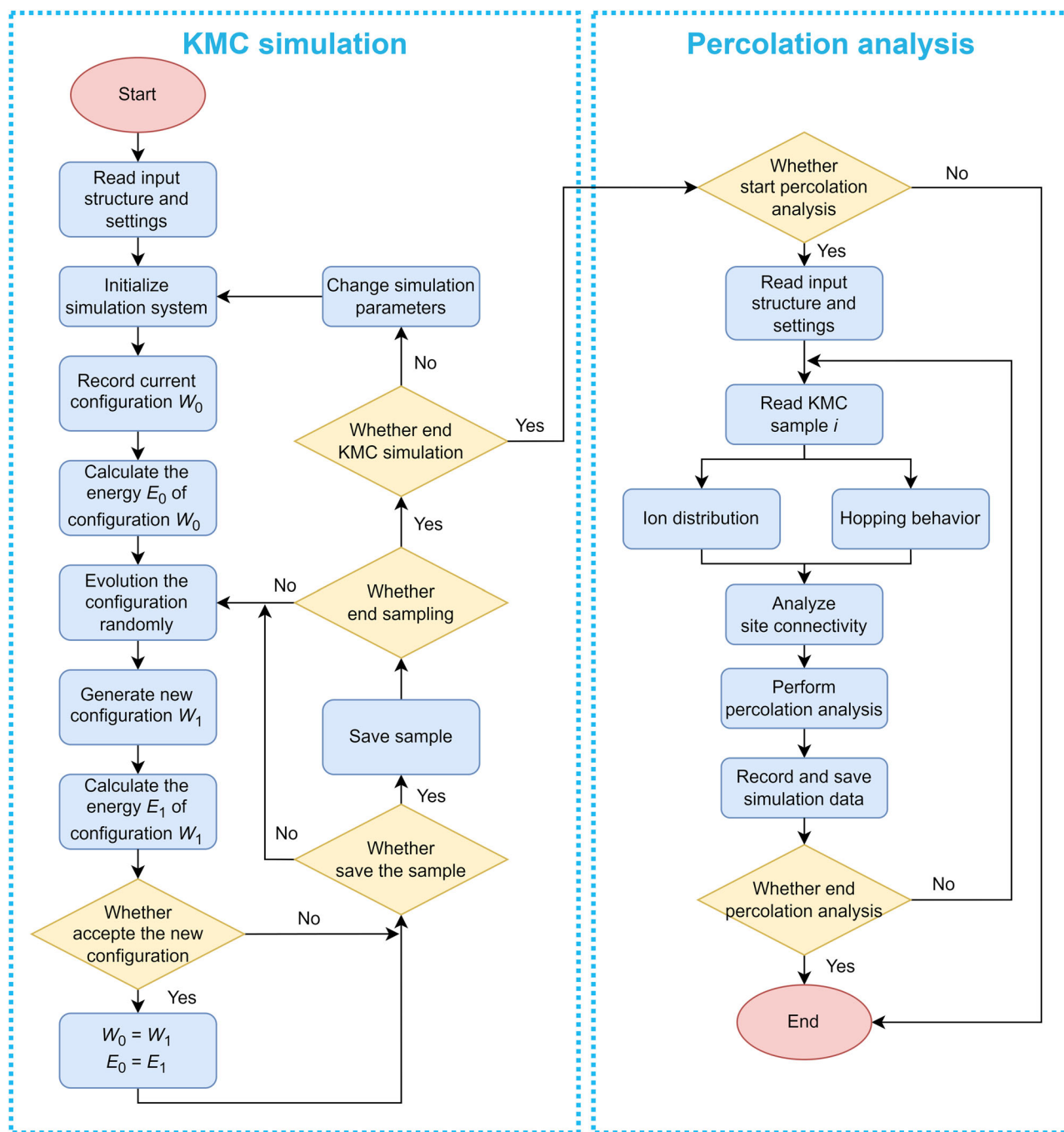
Fig. 4 | Detailed calculation steps of the P-KMC method. The calculations consist of two parts: KMC simulation and percolation analysis, with the former providing inputs for the latter.

ions, and the interactions between nearest neighboring Li ions[32]:

$$E = \sum_{i=1}^{n} E_{\text{site}_i} k_i + \frac{1}{2} \sum_{j=1}^{n} \sum_{\substack{i=1 \\ i \neq j}}^{n} E_{\text{nn}} k_{ij} \qquad (1)$$

where n is the number of Li sites, E_{site_i} is the energy associated with occupying of site i, E_{nn} is the interaction energy between the nearest Li ions, and the values of k_i and k_{ij} depend on the specific ion arrangement. If site i is occupied, $k_i = 1$; otherwise, $k_i = 0$. If site i and its neighbor site j are simultaneously occupied, $k_{ij} = 1$; otherwise, $k_{ij} = 0$. To determine the evolution direction of KMC simulations, the jumps are first randomly

selected in a Monte Carlo step (MCS) to generate a new configuration. Subsequently, the transition probability from configuration a to configuration b ($P_{a \to b}$) is calculated using the scheme proposed by Metropolis et al.[53,54]:

$$P_{a \to b} = \begin{cases} 1 & \Delta E_{a \to b} \leq 0 \\ \exp\left(\frac{-\Delta E_{a \to b}}{k_B T}\right) & \Delta E_{a \to b} > 0 \end{cases} \qquad (2)$$

where k_B is the Boltzmann constant, T is the simulated temperature, and $\Delta E_{a \to b}$ is the energy difference between configurations a and b ($\Delta E_{a \to b} = E_b - E_a$). To facilitate the calculation of time-dependent properties, we adopt one Monte Carlo step as the time unit, thereby

avoiding computationally expensive calculations of real time[32–34]. Considering the possibility of correlated jumps[24–27,55], we classify jump modes into the following types: (1) single-ion jump, where the movement of an ion is independent of adjacent ones; (2) two-ion correlated jump, where two adjacent ions hop simultaneously (as illustrated in Fig. 1b); and similarly (3) three-ion and (4) four-ion correlated jumps. The correlated jumps involving more than four ions are disregarded due to their infrequent occurrence. To quantify the probability and significance of each jump mode, the percentage of jump mode (P_i) is defined as the ratio of the number of i-ion jumps (n_i) to the total number of jumps (n_{tot}): $P_i = \frac{n_i}{n_{tot}}$, where $i = 1, 2, 3, 4$.

Percolation analysis

The configuration samples generated by KMC simulations are utilized to construct a series of percolation models, and percolation analysis is performed on each model, taking into account the specific jump mode. With the constrain of the site-blocking effect, graph coloring algorithm is proposed to determine the connectivity among sites and identify the percolation clusters that represent long-range diffusion pathways[56]. Ions within these percolated pathways are defined as effective mobile ions. The effective mobile ion concentration (C_e) averaged over n percolation models is calculated as:

$$C_e = \frac{1}{n_{\triangle t}} \sum_{i=1}^{n_{\triangle t}} \frac{N_e}{V} \qquad (3)$$

where $n_{\triangle t}$ is the number of time steps, N_e is the number of effective mobile ions during the i-th time period with a time step of $\triangle t$ (in this work, $\triangle t$ is selected as one Monte Carlo step) and V is the volume of simulated supercell. The calculation of C_e additionally incorporates dynamic ion hopping behavior compared to the current percolation analysis, thus providing more reliable information about diffusion properties. The detailed definitions of C_e and other types of concentrations are presented in Section S1 of the Supplementary Material.

Calculation steps of the P-KMC method

Figure 4 illustrates the detailed calculation steps of the P-KMC method, which includes two parts: KMC simulation and percolation analysis. The calculation steps are as follows:

(1) Read input structure and settings. The input structure file should provide site coordinates and connections, which can be obtained through topological analysis.

(2) Initialize the KMC simulation. Construct the lattice-gas model and set up simulation parameters, including temperature T, Li-ion concentration C_{Li}, supercell size, simulation steps, etc.

(3) Record the initial configuration, denoted as W_0, and calculate its system energy, denoted as E_0.

(4) Make ions randomly jump and generate a new configuration, denoted as W_1, and calculate its system energy, denoted as E_1.

(5) Accept the new configuration with probability P by comparing the energies before and after configuration evolution.

(6) When the energy of configuration reaches a steady value, start collecting and saving sample data, including sample configurations, simulation time, etc.

(7) Change the simulation parameters to repeat the above process, record multiple sets of sample data, and determine whether to end the KMC simulation.

(8) Read external instructions to decide whether to perform percolation analysis. if "Yes", read input settings for percolation analysis; if "No", save the simulation data and end the program.

(9) Read the sample data obtained from the KMC simulation and analyze the ion distribution and hopping behavior.

(10) Analyze the site connections in the sample configuration constructed in step (9) according to the ion distribution and hopping behavior.

(11) Perform percolation analysis on the connectivity map constructed in step (10), and record and save simulation data such as effective mobile ion concentration C_e.

(12) Repeat the above process until all sample data have been processed.

(13) End the program.

Data availability

The authors declare that the main data supporting the finding of this study are available within the article and Supplementary Material files. Extra data are available from the corresponding author upon reasonable request.

Code availability

All source codes are available from the corresponding author upon reasonable request.

References

1. Famprikis, T. et al. Fundamentals of inorganic solid-state electrolytes for batteries. *Nat. Mater.* **18**, 1278–1291 (2019).

2. Randau, S. et al. Benchmarking the performance of all-solid-state lithium batteries. *Nat. Energy* **5**, 259–270 (2020).

3. Zhao, Q., Stalin, S., Zhao, C.-Z. & Archer, L. A. Designing solid-state electrolytes for safe, energy-dense batteries. *Nat. Rev. Mater.* **5**, 229–252 (2020).

4. Viswanathan, V. et al. The challenges and opportunities of battery-powered flight. *Nature* **601**, 519–525 (2022).

5. Schmaltz, T. et al. A roadmap for solid-state batteries. *Adv. Energy Mater.* **13**, 2301886 (2023).

6. Zhao, S. et al. Research progress on the solid electrolyte of solid-state sodium-ion batteries. *Electrochem. Energy Rev.* **7**, 3 (2024).

7. Wang, Y. et al. Design principles for solid-state lithium superionic conductors. *Nat. Mater.* **14**, 1026–1031 (2015).

8. Jun, K. et al. Lithium superionic conductors with corner-sharing frameworks. *Nat. Mater.* **21**, 924–931 (2022).

9. Muy, S. et al. Tuning mobility and stability of lithium ion conductors based on lattice dynamics. *Energy Environ. Sci.* **11**, 850–859 (2018).

10. Bachman, J. C. et al. Inorganic solid-state electrolytes for lithium batteries: mechanisms and properties governing ion conduction. *Chem. Rev.* **116**, 140–162 (2016).

11. Wu, T.-T. et al. Garnet-type solid-state electrolytes: crystal structure, interfacial challenges and controlling strategies. *Rare Met* **42**, 3177–3200 (2023).

12. Wu, J. et al. A review on structural characteristics, lithium ion diffusion behavior and temperature dependence of conductivity in perovskite-type solid electrolyte Li$_{3x}$La$_{2/3-x}$TiO$_3$. *Funct. Mater. Lett.* **10**, 1730002 (2017).

13. Zhang, Z. et al. New horizons for inorganic solid state ion conductors. *Energy Environ. Sci.* **11**, 1945–1976 (2018).

14. Wang, Y. et al. Accelerated strategy for fast ion conductor materials screening and optimal doping scheme exploration. *J. Materiomics* **8**, 1038–1047 (2022).

15. Peng, L. et al. Recent progress on lithium argyrodite solid-state electrolytes. *Acta Phys. Chim. Sin.* **39**, 2211034 (2023).

16. Ramakumar, S., Janani, N. & Murugan, R. Influence of lithium concentration on the structure and Li$^+$ transport properties of cubic phase lithium garnets. *Dalton Trans.* **44**, 539–552 (2015).

17. Thompson, T. et al. A tale of two sites: on defining the carrier concentration in garnet-based ionic conductors for advanced Li batteries. *Adv. Energy Mater.* **5**, 1500096 (2015).

18. Inaguma, Y. & Itoh, M. Influences of carrier concentration and site percolation on lithium ion conductivity in perovskite-type oxides. *Solid State Ionics* **86–88**, 257–260 (1996).

19. Lee, J. et al. Unlocking the potential of cation-disordered oxides for rechargeable lithium batteries. *Science* **343**, 519–522 (2014).

20. Ahmad, M. M. Estimation of the concentration and mobility of mobile Li$^+$ in the cubic garnet-type Li$_7$La$_3$Zr$_2$O$_{12}$. *RSC Adv.* **5**, 25824–25829 (2015).

21. Chen, C., Lu, Z. & Ciucci, F. Data mining of molecular dynamics data reveals Li diffusion characteristics in garnet Li$_7$La$_3$Zr$_2$O$_{12}$. *Sci. Rep.* **7**, 40769 (2017).

22. Yu, S. et al. Design of a trigonal halide superionic conductor by regulating cation order-disorder. *Science* **382**, 573–579 (2023).

23. Yu, X., Ma, J., Mou, C. & Cui, G. Percolation structure design of organic-inorganic composite electrolyte with high lithium-ion conductivity. *Acta Phys. Chim. Sin.* **38**, 1912061 (2022).

24. Zou, Z. et al. Relationships between Na$^+$ distribution, concerted migration, and diffusion properties in rhombohedral NASICON. *Adv. Energy Mater.* **10**, 2001486 (2020).

25. He, X., Zhu, Y. & Mo, Y. Origin of fast ion diffusion in super-ionic conductors. *Nat. Commun.* **8**, 15893 (2017).

26. Zhang, Z. et al. Correlated migration invokes higher Na$^+$-ion conductivity in NaSICON-type solid electrolytes. *Adv. Energy Mater.* **9**, 1902373 (2019).

27. Lin, Y.-Y. et al. Isolation of grain versus intergranular transport in Li$_{1+x}$Ti$_x$Ta$_{1-x}$SiO$_5$ suggests concerted ion migration in a high-voltage stable electrolyte from high-throughput descriptors. *ACS Appl. Energy Mater* **6**, 11468–11480 (2023).

28. Yang, Y. & Zhu, H. Effects of F and Cl doping in cubic Li$_7$La$_3$Zr$_2$O$_{12}$ solid electrolyte: a first-principles investigation. *ACS Appl. Energy Mater* **5**, 15086–15092 (2022).

29. Wu, J.-F. et al. Liquid-like Li-ion conduction in oxides enabling anomalously stable charge transport across the Li/electrolyte interface in all-solid-state batteries. *Adv. Mater.* **35**, 2303730 (2023).

30. López, C., Rurali, R. & Cazorla, C. How concerted are ionic hops in inorganic solid-state electrolytes? *J. Am. Chem. Soc.* **146**, 8269–8279 (2024).

31. Gao, Y. et al. Classical and emerging characterization techniques for investigation of ion transport mechanisms in crystalline fast ionic conductors. *Chem. Rev.* **120**, 5954–6008 (2020).

32. Morgan, B. J. Lattice-geometry effects in garnet solid electrolytes: a lattice-gas Monte Carlo simulation study. *R. Soc. Open Sci.* **4**, 170824 (2017).

33. Eisele, S. & Grieshammer, S. MOCASSIN: Metropolis and kinetic Monte Carlo for solid electrolytes. *J. Comput. Chem.* **41**, 2663–2677 (2020).

34. Schuett, J., Kuhn, A. S. & Neitzel-Grieshammer, S. Predicting the Na$^+$ ion transport properties of NaSICON materials using density functional theory and Kinetic Monte Carlo. *J. Mater. Chem. A* **11**, 9160–9177 (2023).

35. Deng, Z. et al. Fundamental investigations on the sodium-ion transport properties of mixed polyanion solid-state battery electrolytes. *Nat. Commun.* **13**, 4470 (2022).

36. Van der Ven, A., Ceder, G., Asta, M. & Tepesch, P. D. First-principles theory of ionic diffusion with nondilute carriers. *Phys. Rev. B* **64**, 184307 (2001).

37. Murugan, R., Thangadurai, V. & Weppner, W. Fast lithium ion conduction in garnet-type Li$_7$La$_3$Zr$_2$O$_{12}$. *Angew. Chem. Int. Ed.* **46**, 7778–7781 (2007).

38. Xie, H. et al. Lithium distribution in aluminum-free cubic Li$_7$La$_3$Zr$_2$O$_{12}$. *Chem. Mater.* **23**, 3587–3589 (2011).

39. Thangadurai, V., Narayanan, S. & Pinzaru, D. Garnet-type solid-state fast Li ion conductors for Li batteries: critical review. *Chem. Soc. Rev.* **43**, 4714–4727 (2014).

40. Rivera, A. et al. Percolation-limited ionic diffusion in Li$_{0.5-x}$Na$_x$La$_{0.5}$TiO$_3$ perovskites ($0 \leq x \leq 0.5$). *Chem. Mater.* **14**, 5148–5152 (2002).

41. Kim, D.-H. et al. Lithium ion migration pathways in Li$_{3x}$La$_{2/3-x}$□$_{1/3-2x}$TiO$_3$. *Ceram. Int.* **38**, S467–S470 (2012).

42. Mitsuishi, K. et al. Nazca Lines by La ordering in La$_{2/3-x}$Li$_{3x}$TiO$_3$ ion-conductive perovskite. *Appl. Phys. Lett.* **101**, 073903 (2012).

43. Kazakevičius, E. et al. Some aspects of charge transport in Li$_{0.5-x}$Na$_x$La$_{0.5}$TiO$_3$ ($x = 0$, 0.25) ceramics. *Funct. Mater. Lett.* **08**, 1550076 (2015).

44. Sun, Y. et al. Recent progress in lithium lanthanum titanate electrolyte towards all solid-state lithium ion secondary battery. *Crit. Rev. Solid State Mater. Sci.* **44**, 265–282 (2019).

45. Lu, J. & Li, Y. Perovskite-type Li-ion solid electrolytes: a review. *J. Mater. Sci. Mater. Electron.* **32**, 9736–9754 (2021).

46. He, B. et al. A highly efficient and informative method to identify ion transport networks in fast ion conductors. *Acta Mater* **203**, 116490 (2021).

47. Stramare, S., Thangadurai, V. & Weppner, W. Lithium lanthanum titanates: a review. *Chem. Mater.* **15**, 3974–3990 (2003).

48. Huang, J. et al. Non-topotactic reactions enable high rate capability in Li-rich cathode materials. *Nat. Energy* **6**, 706–714 (2021).

49. Abdellahi, A., Urban, A., Dacek, S. & Ceder, G. Understanding the effect of cation disorder on the voltage profile of lithium transition-metal oxides. *Chem. Mater.* **28**, 5373–5383 (2016).

50. He, B. et al. CAVD, towards better characterization of void space for ionic transport analysis. *Sci. Data* **7**, 153 (2020).

51. He, B. et al. High-throughput screening platform for solid electrolytes combining hierarchical ion-transport prediction algorithms. *Sci. Data* **7**, 151 (2020).

52. He, X. et al. Crystal structural framework of lithium super-ionic conductors. *Adv. Energy Mater.* **9**, 1902078 (2019).

53. Metropolis, N. et al. Equation of state calculations by fast computing machines. *J. Chem. Phys.* **21**, 1087–1092 (1953).

54. Metropolis, N. & Ulam, S. The Monte Carlo method. *J. Am. Stat. Assoc.* **44**, 335–341 (1949).

55. Xu, M., Ding, J. & Ma, E. One-dimensional stringlike cooperative migration of lithium ions in an ultrafast ionic conductor. *Appl. Phys. Lett.* **101**, 031901 (2012).

56. Fisher, M. E. & Essam, J. W. Some cluster size and percolation problems. *J. Math. Phys.* **2**, 609–619 (1961).

Acknowledgments

Author contributions

Bowei Pu: Conceptualization (equal); Formal analysis (equal); Investigation (equal); Methodology (equal); Software (equal); Resources (equal); Writing—original draft (equal); Writing—review & editing (equal). Zheyi Zou: Formal analysis (equal); Writing—review & editing (equal); Funding acquisition (equal); Project administration (equal); Resources (equal); Supervision (equal). Jinping Liu: Conceptualization (equal); Formal analysis (equal); Investigation (equal); Methodology (equal); Software (equal); Resources (equal); Writing—original draft (equal); Writing—review & editing (equal). Bing He: Methodology (equal). Dezhi Chen: Writing—review & editing (equal). Da Wang: Writing—review & editing (equal). Yue Liu: Writing—review & editing (equal). Maxim Avdeev: Writing—review & editing (equal). Siqi Shi: Conceptualization (equal); Writing—review & editing (equal); Funding

acquisition (equal); Project administration (equal); Resources (equal); Supervision (equal).

Competing interests

The authors declare no competing interests.

Additional information